



Trans. Nonferrous Met. Soc. China 33(2023) 357-370

Transactions of Nonferrous Metals Society of China

www.tnmsc.cn



Tensile property and microstructure of Al-4.77Mn-1.37Mg-0.67Sc-0.25Zr alloy under different selective laser melting processing parameters

Yi LAI¹, Ying DENG^{1,2}, Xin-wen ZHU¹, Yi-fan GUO¹, Guo-fu XU^{1,2}, Ji-wu HUANG¹, Zhi-min YIN¹

- 1. School of Materials Science and Engineering, Central South University, Changsha 410083, China;
- 2. State Key Laboratory of Powder Metallurgy, Central South University, Changsha 410083, China

Received 8 October 2021; accepted 11 April 2022

Abstract: A new Al–4.77Mn–1.37Mg–0.67Sc–0.25Zr alloy (wt.%) was prepared by selective laser melting (SLM) technique under different processing parameters, and the microstructure and mechanical property of the SLM alloys were investigated by tensile tests and microscopy methods. The results show that when the energy density ranges from 104 to 143 J/mm³, the mechanical properties remain relatively stable. The yield strength, ultimate tensile strength and elongation are 335–338 MPa, 397–400 MPa and above 11%, respectively. Meanwhile, few defects and coarse intermetallics form and lots of fine AlFeMnScZr phases precipitate. When the energy density exceeds 152 J/mm³, some cavities and cracks can be observed, and elongation decreases sharply. The quantitative calculation results show that the solid solution strengthening, grain boundary strengthening and precipitation strengthening account for 44%, 41% and 15%, respectively.

Key words: selective laser melting; aluminium alloys; tensile property; strengthening mechanism; microstructure

1 Introduction

Additive manufacturing (AM), commonly known as 3D printing, has become an advanced technology for manufacturing complex geometries close to their net shape [1-4]. The most widely used AM technology is selective laser melting (SLM). During the SLM process, a high-energy laser beam selectively melts the powder layer and the solid components accumulate [5-8]. As SLM can directly manufacture complex structures, the production efficiency and the manufacturing precision improve significantly. In addition, compared with the traditional manufacturing processing, SLM technology greatly reduces the waste of raw materials and has many environmental advantages [9].

Compared with the cast aluminum alloys, selective laser melting aluminum alloys have more product defects, such as porosity and cracks. Therefore, their mechanical property and fatigue life are inferior to the cast alloys [10]. Scanning speed and laser power in the SLM process have significant influence on the quality of 3D printed samples [11]. Many scholars have done a lot of relevant research on improving the mechanical property of SLM aluminum alloy by optimizing SLM processing parameters. The SLM parameters are related to the energy absorbed by the molten pool in the SLM process, thus affecting the solidified microstructure [12]. BAYOUMY et al [13] prepared the Al-Mn-Mg-Sc-Zr alloys with different laser powers and scanning speeds, and they finally concluded that the alloys prepared under 350 W and 1600 mm/s had the best properties. By

optimizing SLM process parameters, the porosity of 3D printed samples can be reduced [14]. KEMPEN et al [15] optimized a set of SLM process parameters and obtained AlSi10Mg alloy samples with fine microstructure and good mechanical properties comparable to casting materials.

Currently, material researchers focus on developing SLMed aluminum alloys with a good performance by alloying design. LI et al [16] conducted a study on the Al-6.2Mg-0.36Sc-0.09Zr alloy sample prepared by SLM, and the results showed that the alloy had high compressive strength up to 390 MPa. WU et al [17] studied the effect of melting mode on mechanical properties during the preparation of AlSi10Mg alloy by SLM. The results show that the alloy with high tensile properties (tensile strength 458 MPa, yield strength 293 MPa, and elongation 7.7%) can be obtained under the transition mode. LI et al [18] developed a new Si- and Zr-modified Al-Zn-Mg-Cu (Al7075) alloy powder for SLM and obtained excellent tensile properties (tensile strength 446 MPa, elongation 6.5%) of the SLM alloy sample. The above results show that good alloying design is the basis of achieving superior performance.

In this work, we design a new SLM Al-Mn-Mg-Sc-Zr alloy and try to obtain high strength and good ductility by optimization of SLM processing parameters. Based on the above, the detailed microstructure will be characterized to clarify the main strengthening mechanisms.

2 Experimental

2.1 SLM powder and method

Table 1 shows the compositions of the SLM aluminum alloy powder. The morphology of the metal powders was observed on a Nova nanoSEM430 field emission scanning electron microscope, and the results are shown in Fig. 1. It can be seen from Fig. 1(a) that most of the powders are spherical and only a few irregular ellipsoidal powders exist. Besides, few powders adhere to the surface of large powders in the high-magnification SEM image (Fig. 1(b)). Figure 1(c) shows the particle size distribution of SLM powders, obtained from the Mastersizer 3000 laser particle size analyzer. It can be seen that the particle size ranges from 4 to 40 μm. The median size of particle is 22.4 μm, the mean size is 26.1 μm and the particle

size difference is small. Particle size up to $14.1 \mu m$ accounts for 10% and particle size up to $35.7 \mu m$ accounts for 90% of particles.

Table 1 Chemical compositions of SLM alloy powder (wt.%)

Mg	Mn	Fe	Sc	Zr
1.37	4.77	0.052	0.67	0.25
Si	Cr	Ti	Zn	Al
0.10	0.0050	0.0022	0.0044	Bal.

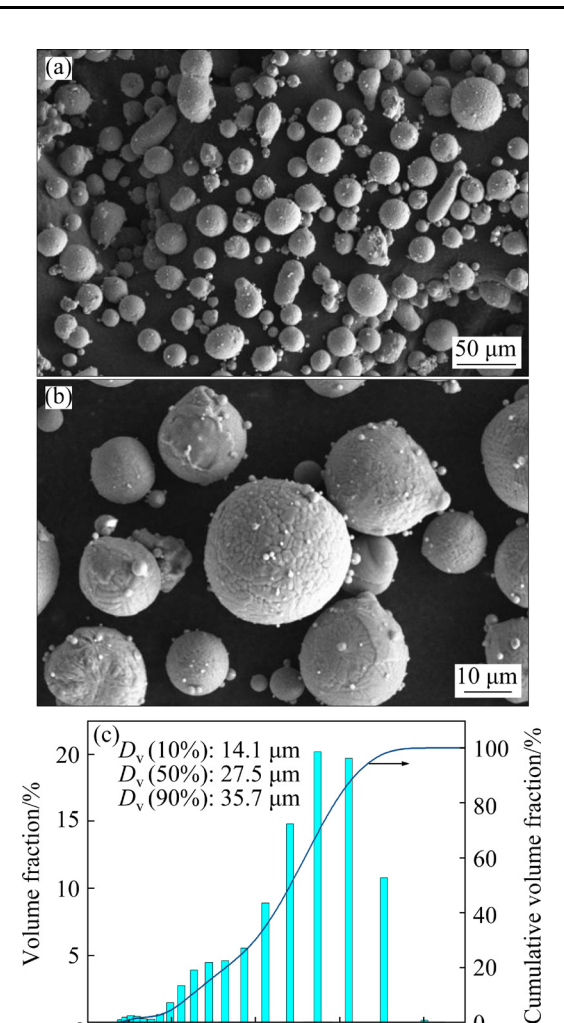


Fig. 1 SEM images (a, b) and size distribution (c) of SLM metal powder

Particle diameter/µm

40

In this work, the SLM process parameters were optimized by comparing the performance of aluminum alloy printed at different laser powers (310, 330, 350, 370 W) and scanning speed (800, 900, 1000, 1100 mm/s). The scan strategy is shown in Fig. 2. Other major technological parameters in the SLM process are: the layer thickness 0.03 mm,

the scanning spacing 0.02 mm, the hatch distance 0.09 mm, the stripe width 5 mm, and the preheating temperature 35 °C. Four SLM parameters, laser power, scanning speed, scanning spacing and layer thickness, can be comprehensively reflected by energy density [19], and their relationship is as follows:

$$E = \frac{P}{Vht} \tag{1}$$

where E is the energy density (J/mm³), P is the laser power, h is the scanning spacing, t is the layer thickness, and V is the scanning speed. Combined with the SLM parameters selected in this experiment, the energy density of 16 samples was calculated as listed in Table 2.

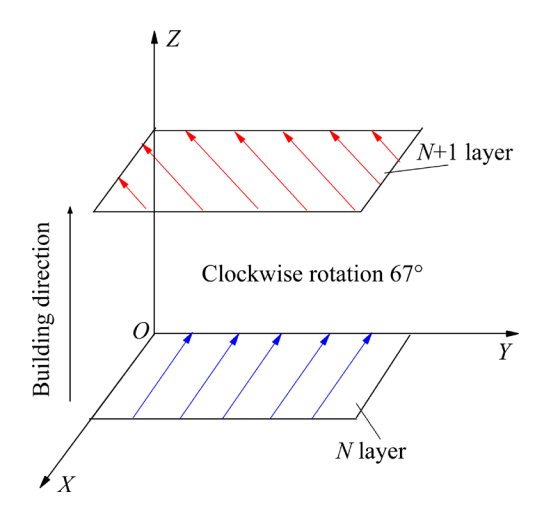


Fig. 2 SLM scanning strategy

2.2 Hardness and tensile test methods

Samples for hardness tests were mechanically ground with 600-1600 grit paper and polished with $1.5 \,\mu m$ diamond pulp, and finally measured on an HVT-1000A Vickers micro-hardness tester (loading force F=1.96 N, loading time t=15 s). Three hardness values for each sample were obtained, and the average values and the standard deviations are present in this paper.

The tensile test samples were fabricated directly by SLM. Their dimensions are shown in Fig. 3. MTS 810 tensile testing machine was used for obtaining mechanical properties at room temperature and the tensile speed was 1 mm/min. Besides, the direction of the tensile test sample is perpendicular to the building direction. The corresponding ultimate tensile strength (σ_b), yield strength ($\sigma_{0.2}$) and elongation (δ) are obtained.

Table 2 Energy density and hardness of SLM samples under different process parameters

Sample No.	P/W	V/ (mm·s ⁻¹)	Energy density/ (J·mm ⁻³)	Hardness (HV)
1	310	800	143	116±0.8
2	310	900	127	117±0
3	310	1000	114	118±1.4
4	310	1100	104	120±0.6
5	330	800	152	113±1.3
6	330	900	135	123±1.3
7	330	1000	122	120±1.4
8	330	1100	111	121±0.8
9	350	800	162	117±1.3
10	350	900	144	119±1.6
11	350	1000	129	120±1.3
12	350	1100	117	119±1.3
13	370	800	171	115±0.7
14	370	900	152	118±1.3
15	370	1000	137	117±1.3
16	370	1100	124	117±1.7

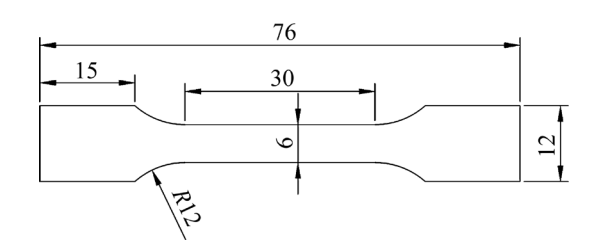


Fig. 3 Dimensions of tensile samples (unit: mm)

2.3 Microstructure characterization methods

A Nikon LV150N optical microscope (OM) with 220V/50Hz power was used to observe and analyze the defects of 3D-printed aluminum alloys. The fracture morphology of the failed samples and the distribution of elements on the surface of the tensile specimens were analyzed on a Zeiss EVO10-3412 scanning electron microscope and an X-MAX50 energy spectrometer. The phase identification was conducted on a D8 ADVANCE X-ray diffractometer (XRD) with a scanning speed of 2 (°)/min (Cu K_{\alpha} radiation, λ =0.154 nm). Grain size, morphology and phase distribution of 3D-printed aluminum alloys were observed on a Titan G² 60-300 field emission projection electron microscope with spherical aberration correction. EBSD specimens were characterized on an FEI

Helios nano-lab 600i scanning electron microscope (SEM), equipped with an EBSD detector (Oxford, NordlysMax2), operating at 20 kV, with a scanning step size of 1.4 μ m.

3 Results

3.1 Effects of SLM processing parameters on defects and hardness

Figure 4 shows the OM images of the surface of 16 SLM samples. Sample 10 has the largest cavity size and density, followed by Samples 5, 13 and 15. Samples 1, 7 and 11 have fewer and smaller cavities. Unlike the other samples, the obvious crack can be observed in Sample 2. On the whole, Samples 4, 6, 8 and 16 have good SLM quality. At the same laser power, when the scanning speed is low, there are many large holes. When the scanning speed increases, the number of large holes decreases, but the number of small holes increases. Considering both scanning speed and laser power, with the increase of energy density, the number of holes increases. This is because the alloy powders absorb too much energy in the molten pool under the high energy density condition, and the liquid

metal moves violently and causes sputtering, forming cavities.

Figure 5 shows the influence of scanning speed and laser power on sample hardness. The hardness is listed in Table 2. The results show that, with the increase of scanning speed, the sample hardness firstly increases and then decreases (Fig. 5(a)). When the laser power increases, the hardness of the samples increases first and then decreases (Fig. 5(b)). Sample 6 (135 J/mm³) has the highest hardness (HV 123), followed by Sample 8 (111 J/mm³) with HV 121. The hardness of the Sample 5 (152 J/mm³) is the lowest, only HV 113. Within the energy density scope of 104-143 J/mm³, the hardness is in a stable range of HV 117 to HV 123. When the energy density is higher than 152 J/mm³, the hardness is lower than HV 115.

The above hardness results can be explained by the following reasons. When the energy density is low, the molten pool absorbs insufficient energy. Therefore, the alloy powder does not have enough energy to melt completely, and it is easy to form pores, cracks and other defects, leading to low hardness. However, when the energy density is too

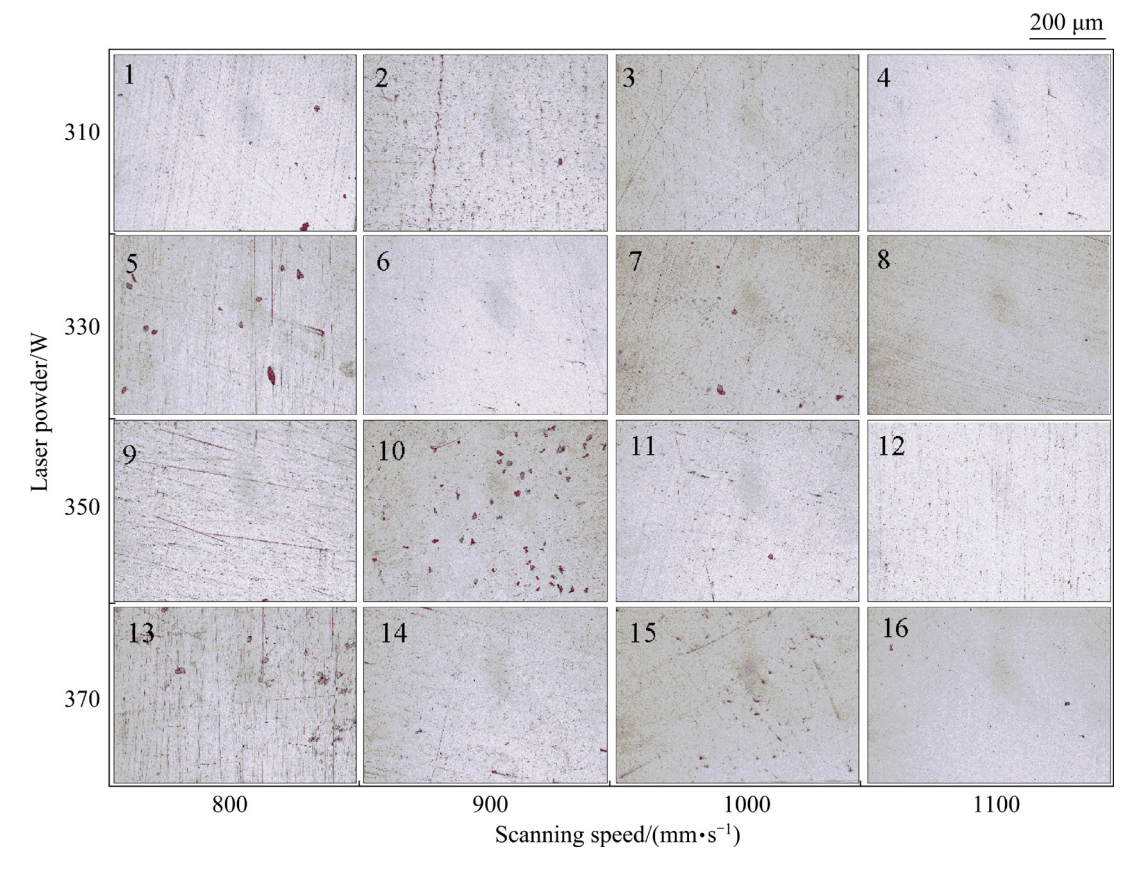


Fig. 4 OM images of Samples 1-16

high, the powder layer absorbs too much energy, which makes the liquid alloy in the molten pool move violently and produce spheroidization [20,21], reducing the hardness. Therefore, the selection of energy density should be in a suitable range. In this case, the metal powder can be melted completely, and the generation of defects reduces, improving the hardness of the samples.

3.2 Effects of SLM processing parameters on surface roughness

Combined with OM and hardness results, the samples produced under typical SLM processing parameters were selected for the subsequent characterization. Figure 6 shows the three-dimensional surface morphology of samples. The surface morphology of Samples 1, 5, 6 and 8 is

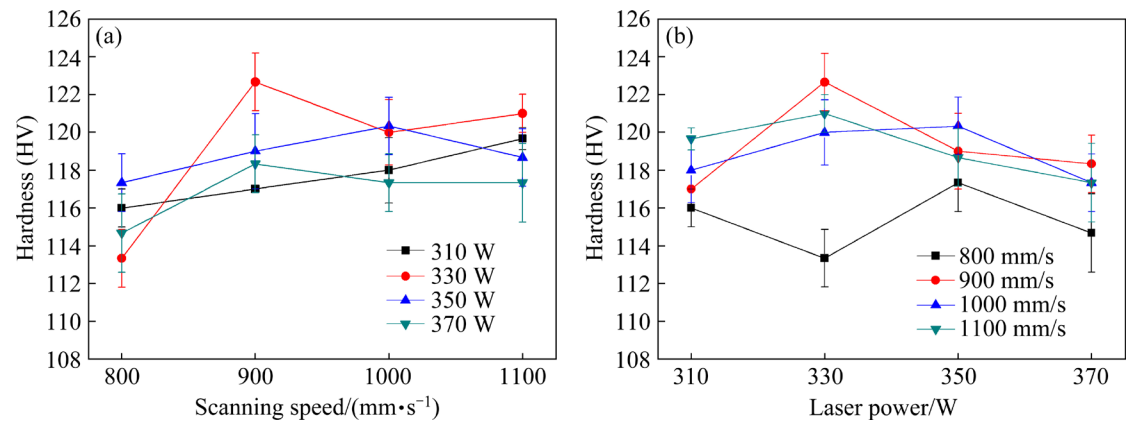


Fig. 5 Influence of scanning speed (a) and laser power (b) on hardness of SLM samples

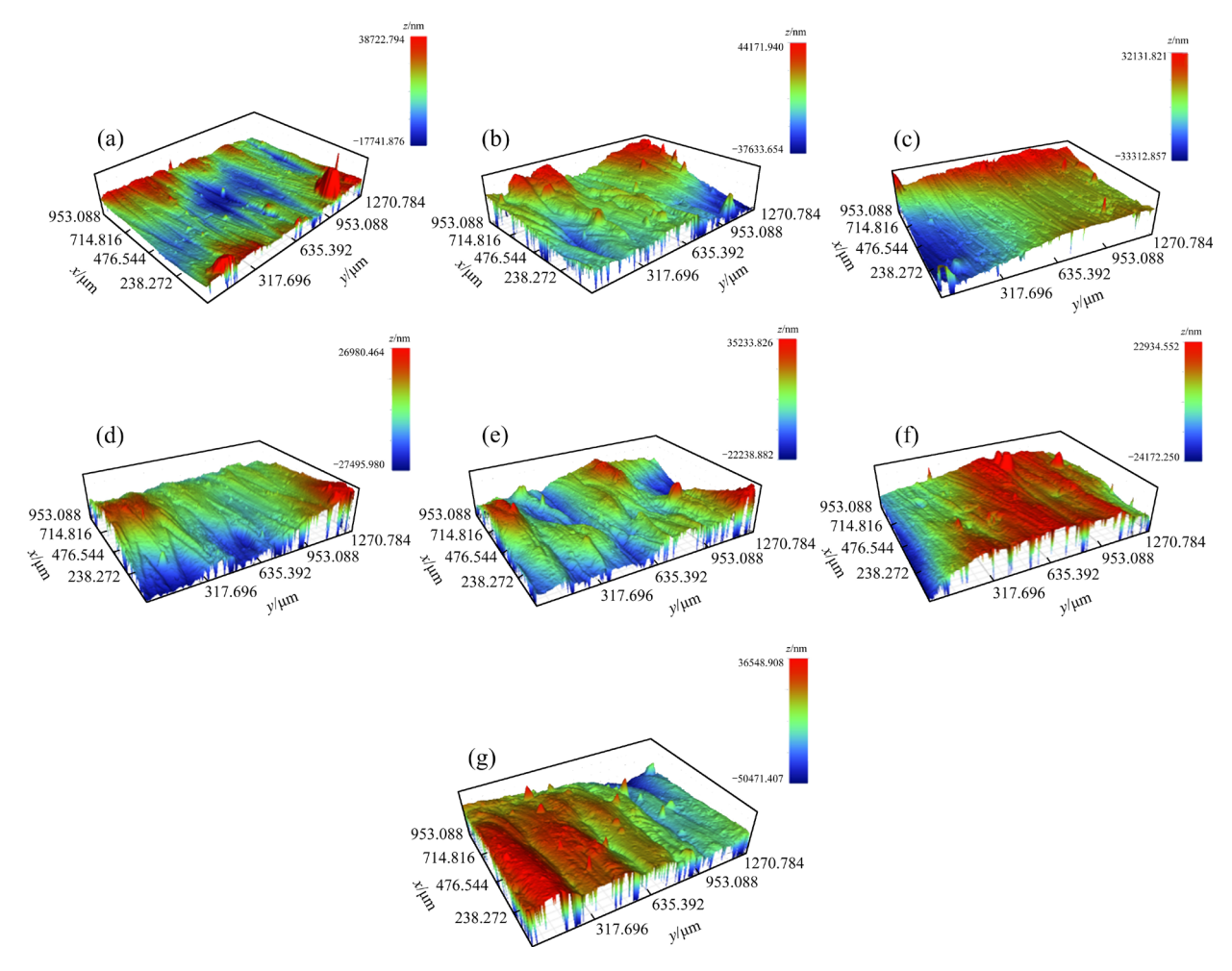


Fig. 6 Three-dimensional surface morphology of different samples: (a) Sample 1; (b) Sample 4; (c) Sample 5; (d) Sample 6; (e) Sample 8; (f) Sample 13; (g) Sample 16

smooth (Figs. 6(a, c, d, e)), while some sharp protrusions can be seen on the surface of Samples 4, 13 and 16 (Figs. 6(b, f, g)). Figure 7 shows the roughness changes with energy density. The red zone is the roughness of the samples with a speed of 1100 mm/s, and the green zone is the roughness of the samples with a speed of 800 mm/s. It is obvious that the surface roughness increases with the increase of scanning speed. When the scanning speed is the same, the roughness of the sample is close to each other and increases slightly with the increase of energy density. In conclusion, scanning speed is the main influencing factor of surface roughness. This is because at high scanning speed, residual metal powder particles are not completely melted and adhere to the sample surface after SLM processing, which increases roughness.

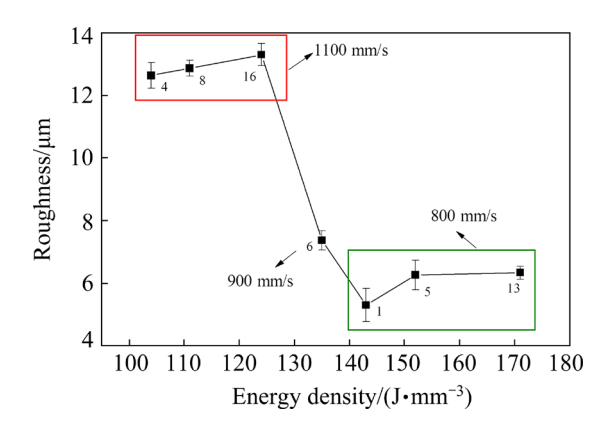


Fig. 7 Influence of energy density on surface roughness

3.3 Effects of energy density on mechanical property and fracture morphology

Figure 8 shows the stress-strain curves of typical SLM samples. The yield strength, ultimate tensile strength and elongation are listed in Table 3. As can be seen from the stress-strain curves, the strength and elongation of Sample 13 (171 J/mm³) are the lowest. The highest yield strength is up to 338 MPa (Sample 8). The highest ultimate tensile strength is 400 MPa (Sample 6). The maximum elongation is 14.8% (Sample 8). When the energy density ranges from 104 to 143 J/mm³, the mechanical properties remain relatively stable. The yield strength, ultimate tensile strength and elongations are 335-338 MPa, 397-400 MPa and above 11%, respectively, indicating that the mechanical properties remain relatively stable in this energy density range. The elongation of

samples with a high energy density is lower than that of samples with a low energy density. When the energy density is higher than 152 J/mm³, the elongation decreases sharply, only 6%–8%.

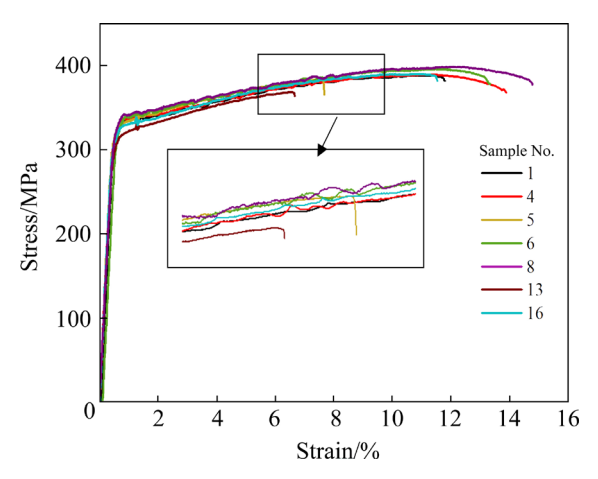


Fig. 8 Stress-strain curves under different SLM processing parameters

Table 3 Influence of energy density on mechanical properties of SLM specimens

Sample No.	Energy density/ (J·mm ⁻³)	Yield strength/ MPa	Tensile strength/ MPa	Elongation/
1	143	335±0.7	397±1.4	11.9±0.6
4	104	336±1.1	397±1.6	13.7±0.7
5	152	334±0.5	390±0.7	8.4 ± 0.3
6	135	336±1.2	400±0.8	13.4±0.4
8	111	338±0.6	397±1.0	14.8 ± 0.5
13	171	332±0.9	369±1.1	6.3 ± 0.4
16	124	335±0.5	398±0.7	11.3±0.5

Figure 9 shows the SEM fracture morphology of the tensile samples. The results indicate that the fracture surface of Samples 1, 4, 6, 8 and 16 with low energy density (Figs. 9(a, b, d, e, g)) have only a few holes, and Sample 6 (135 J/mm³) has the least holes. Samples 5 and 13 (Figs. 9(c, f)) with higher energy density have a large number of cavities on the fracture surface with sizes ranging from 35 to 130 µm, and a few microcracks are also found. It can be seen that the porosity of SLM aluminum alloy increases with the increase of energy density. This is because the energy density is too high, and the alloy powder absorbs too much energy per unit time during SLM processing, which leads to the spheroidization of the molten pool and the formation of cavities and microcracks.

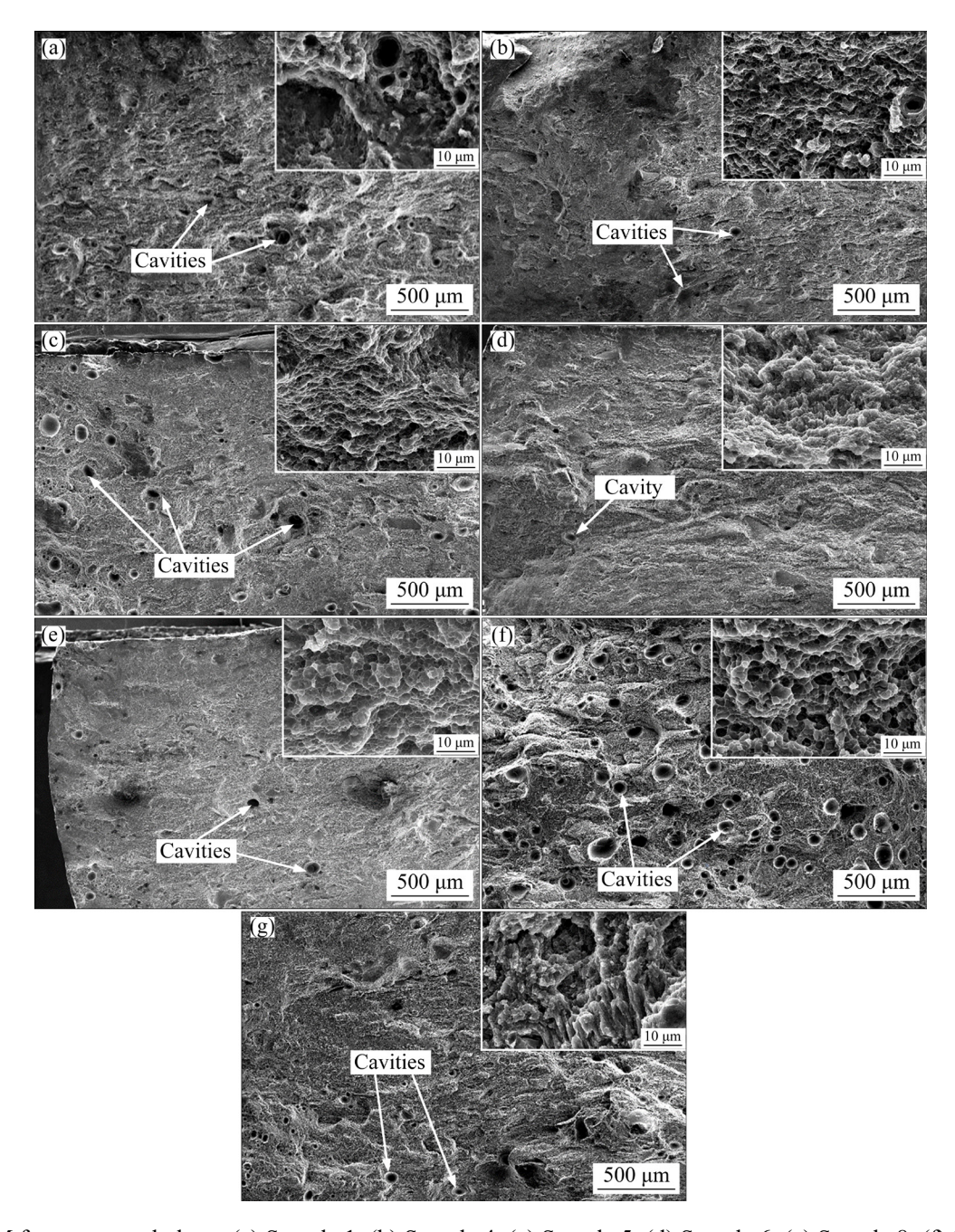


Fig. 9 SEM fracture morphology: (a) Sample 1; (b) Sample 4; (c) Sample 5; (d) Sample 6; (e) Sample 8; (f) Sample 13; (g) Sample 16

In the amplified fracture images of the samples, it can be seen that there are a lot of dimples on the fracture surface, which indicates that the samples have the characteristics of ductile transgranular fracture. SEM results verify that the elongation is mainly affected by the original defects such as cavities and microcracks. This is because the defects can result in local stress concentration during the tensile process. The plastic deformation of the matrix and the formation of dimples between the adjacent holes connect the holes, leading to the

appearance of microcracks, which further extend to the entire surface and cause the fracture of the material. SEM results are in agreement with the literature [22,23].

3.4 Effects of energy density on phase, intermetallics, element distribution, grains and microtextures

Figure 10 shows XRD results of alloy powders and SLMed alloys. The results indicate that only four α (Al) diffraction peaks, Al(111), Al(200),

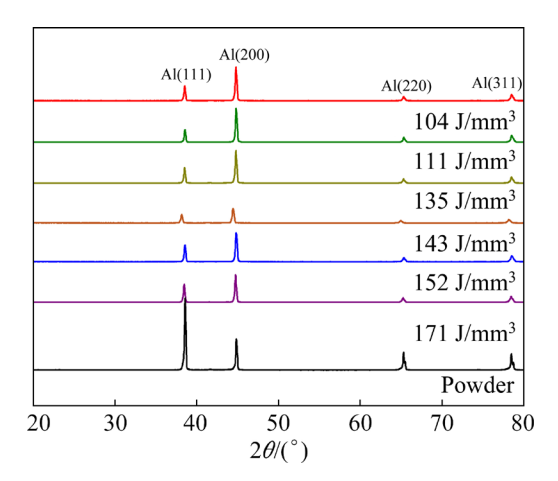


Fig. 10 XRD patterns of powders and SLM alloys

Al(220) and Al(311) can be detected. Compared with the alloy powder, the strongest Al peak of the sample prepared by SLM changes from (111) to (200). This is because the grains formed in the SLM process grow preferentially along the (200) direction. Compared with the metal powder, the peak position of SLM alloy is shifted to the left. And with the decrease of energy density, the diffraction angle of the Al (200) diffraction peak gradually shifts to a lower angle. This may be due to the solid solubility of alloying elements in the aluminum matrix during the SLM process, and the increase of crystal plane spacing and cell parameters, leading to lattice distortion. According to the diffraction equation, the diffraction angle tends to be lower. In addition, the half-width of the molded sample did not change, indicating that the grain size did not increase significantly. It can be seen that the diffraction intensities of the three samples with the lowest energy density are all large, indicating that the Al phase has good crystallinity with these energy densities.

Figure 11 shows the backscattered electron scanning images and EDS results of intermetallics. It can be seen that there are some small cavities and coarse intermetallics on the SLM sample surface. Samples 1, 4, 6 and 8 (Figs. 11(a-d)) have a few pores and small pore size. Figure 11(e) shows that there are many cavities with large size. This result is consistent with the surface morphology of the tensile fracture above. In addition, a large number of irregular coarse intermetallics are found on the surface of the samples. Sample 13 (171 J/mm³) has the most intermetallics, the largest phase size and the most concentrated distribution. In other four samples, the distribution of intermetallics is more dispersed than that in Sample 13, and the number of intermetallics is much less than that of Sample 13. Among them, the intermetallics of Sample 6 are the least and almost invisible in the matrix. According to the EDS results (Fig. 11(f)), the intermetallics consist of 10.2% Mn and a small amount (less than 1%) of Mg and Sc. Surface scanning results of Sample 6 are shown in Fig. 12. Al, Mn, Mg and other main elements on the sample surface are evenly distributed without macroscopic segregation.

The concentrated distribution of intermetallics increases the possibility of crack formation in the alloy subjected to external stress [24], and the interlacing of cavities and intermetallics makes it easier to form microcracks. Therefore, Samples 1, 4,

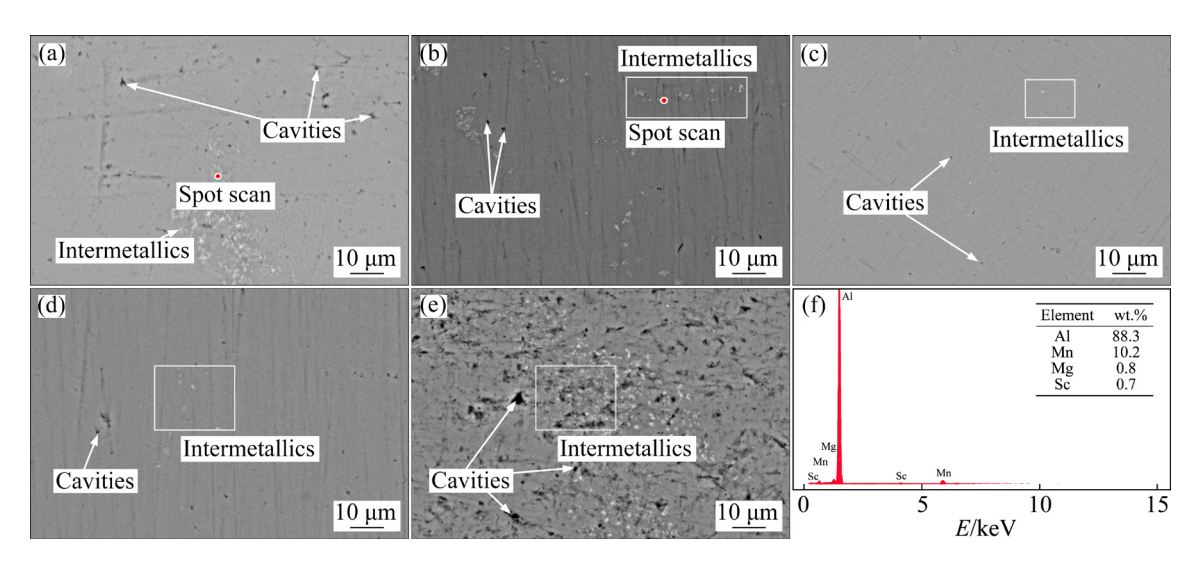


Fig. 11 SEM images (a–e) and corresponding EDS results (f): (a) Sample 1; (b) Sample 4; (c) Sample 6; (d) Sample 8; (e) Sample 13

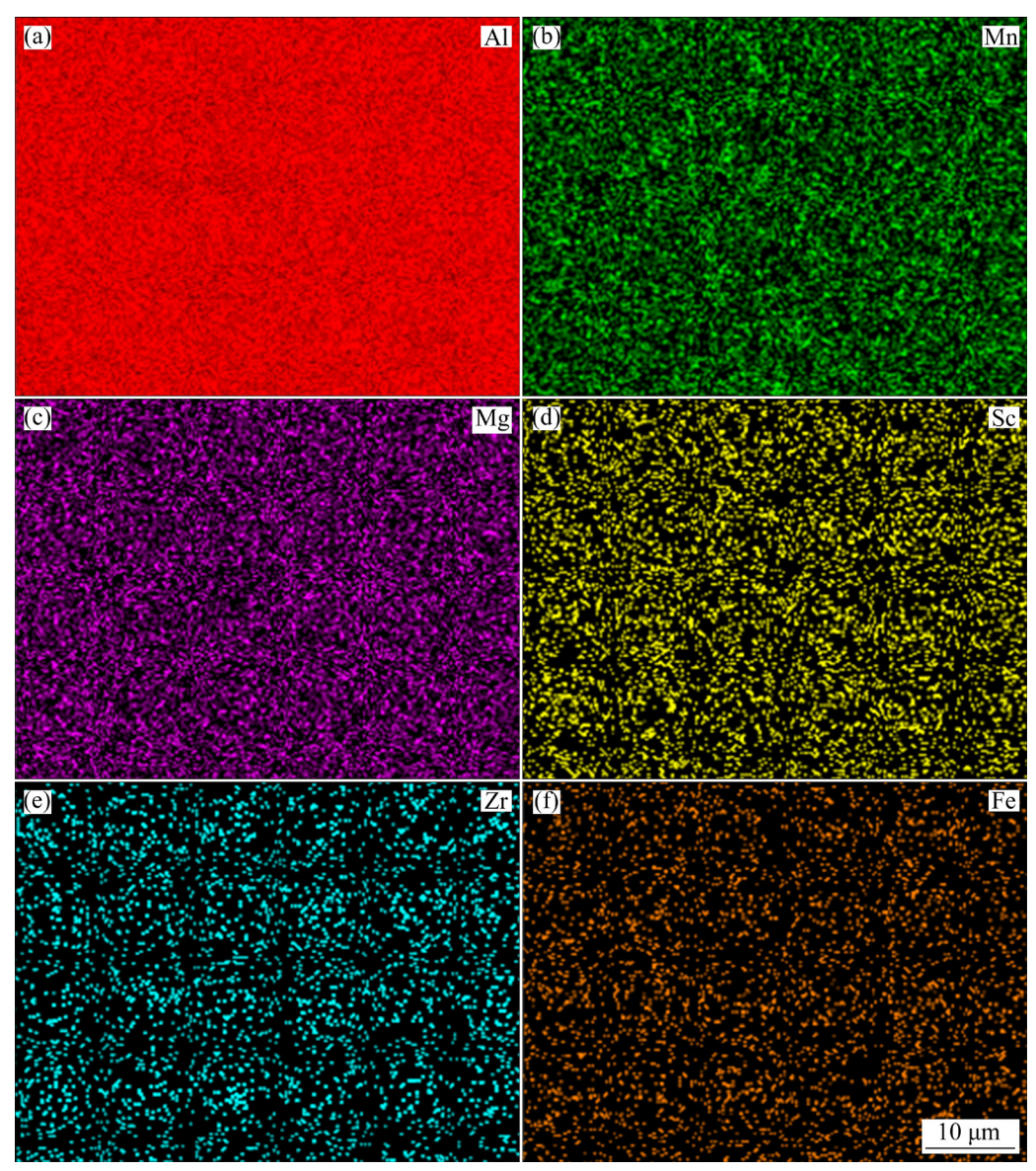


Fig. 12 Element distribution maps of Sample 6

6 and 8 (energy density between 104 and 143 J/mm³) with fewer and dispersed intermetallics are less likely to form microcracks due to the stress concentration and exhibit better tensile properties.

By comprehensive analysis of the above experimental results, it can be seen that the samples with energy density of 104–143 J/mm³ have good properties and few defects. To further study their microstructure, TEM, HAADF-STEM and EDS Chemi-STEM mapping scanning images of Sample 6 with an intermediate energy density (135 J/mm³), are shown in Fig. 13. The grain size of Sample 6 is 0.8–2.1 µm. Figure 13(b) shows that the precipitated phase is uniformly distributed in the grains, and its size ranges from 60 to 90 nm. STEM-EDS results (Figs. 13(c–h)) further indicate

that the precipitate is the AlMnFeScZr phase.

Figure 14 shows the EBSD maps and pole figures of Samples 4, 6 and 13. The building direction (BD) is shown in Fig. 14. Three samples all consist of columnar crystals and equiaxed grains. Columnar grains are at the central area of the molten pool, growing along the building direction. The width of columnar grains is $2-10 \, \mu m$. Equiaxed grains are at the bottom of the molten pool with a grain size of $1-3 \, \mu m$, which is the fine-grain zone. The grain size of Sample 4 (Fig. 14(a)) in the fine-grain region is less than $1 \, \mu m$, and the grain width of the columnar grain region is $4-7 \, \mu m$. The grain diameter of Sample 6 (Fig. 14(b)) is $1-3 \, \mu m$ in the fine-grain zone and $2-5 \, \mu m$ in the columnar grain zone. Sample 13

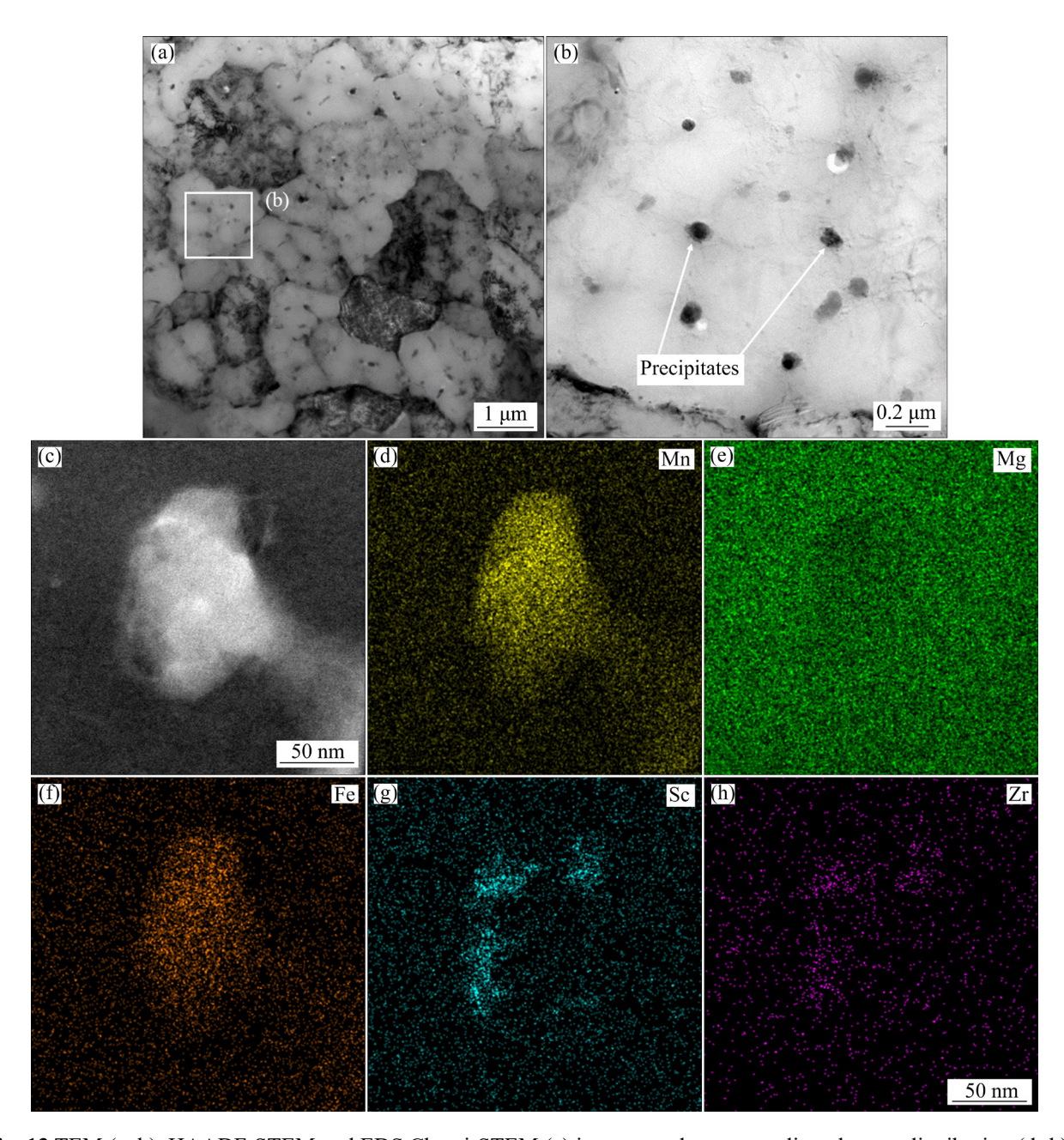


Fig. 13 TEM (a, b), HAADF-STEM and EDS Chemi-STEM (c) images, and corresponding element distribution (d-h)

(Fig. 14(c)) also has very fine grains in the fine grain zone, about 1 μ m, with fewer columnar grains and a grain width of 4–10 μ m. Comparing the EBSD of the three samples, the grain size of Sample 13 is the smallest, but there is a great difference in grain size between fine and columnar grain regions. The grain diameter of Sample 6 is relatively average. In addition, Samples 4 and 6 have obvious molten pool structures.

According to the microstructure characterization and pole figures of the columnar and equiaxed regions of Sample 6 (Figs. 14(d, e)), it is found that the columnar crystal has an obvious

preferred orientation, while the grain orientation in the equiaxed crystal region is random. This is because there is a large thermal gradient in the molten pool during the SLM manufacturing process. When the laser melts the metal powder, a large number of small grains nucleate at the edge of the molten pool. The grains in the direction of (100) preferentially grow to the center of the molten pool and form columnar grains. Other grains still exist as equiaxed grains at the edge of the molten pool. Therefore, the texture of Samples 4 and 6 with obvious columnar crystals is stronger than that of Sample 13 with a large equiaxed crystal region.

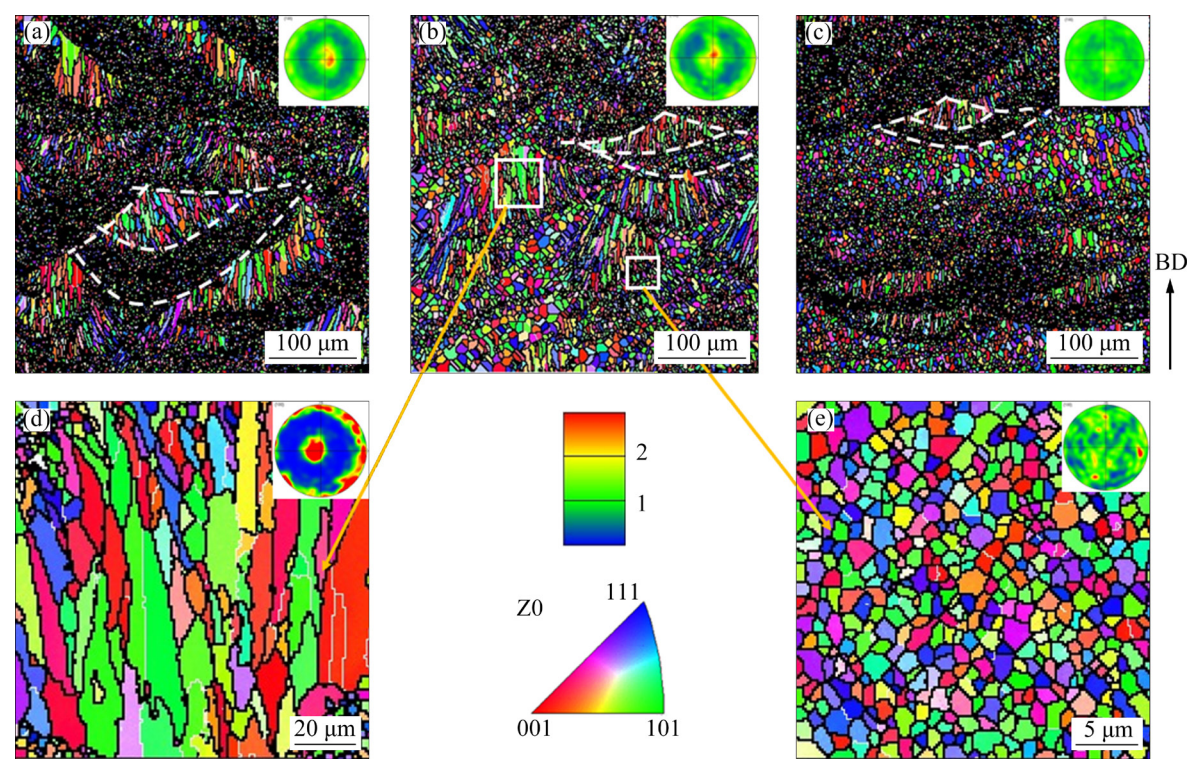


Fig. 14 EBSD maps and pole figures: (a) Sample 4; (b) Sample 6; (c) Sample 13; (d) Bottom of molten pool; (e) Central area of molten pool

4 Discussion

4.1 Proper selective laser melted processing parameters

According to the experimental data obtained in this work, the defects, microstructure and mechanical properties of 3D-printed aluminum alloy are related to SLM parameters. Therefore, the influence of laser power and scanning speed should be considered to optimize the SLM process parameters, and the energy density should be analyzed comprehensively.

During the SLM process, it is easy to form lots of defects. Firstly, the inert gas getting into the molten pool is too late to escape and form cavities [25]; Secondly, the absorption energy of the molten pool is too low to make the powder melt completely, which is easy to form cavities. Thirdly, the molten pool absorbs too much energy, leading to violent convection of internal liquid metal and sputtering, and finally forming holes. From the above experimental results, it can be seen that the defect and microstructure of Samples 1, 4, 6, 8, and 16 with energy density of 104–143 J/mm³ are similar. There are a few pores, microcracks and

coarse intermetallics formed in the SLM process. And they have fine grains and uniform distribution of elements. The strength performance is also excellent and stable within this energy density. Therefore, the energy density between 104 and 143 J/mm³ is a good SLM processing range.

4.2 Strengthening mechanisms

In the SLM process, when the scanning speed is high, the laser beam stays on the molten pool for less time. Therefore, the molten pool absorbs less energy. In this case, the temperature is low, and the cooling speed is accelerated, resulting in the limited diffusion and growth of grains. As can be seen from Figs. 12 and 13, the solute elements are almost dissolved into the matrix in the SLMed alloys. According to Formula (2) [26], the contribution of solution strengthening to strength improvement $\sigma_{\rm SSS}$ can be obtained:

$$\sigma_{\rm SSS} = \sum_{i} A_i C_i^{\beta_i} \tag{2}$$

where A_i is the solid solution-enhanced constant element of the various solute elements, C_i represents the concentration of each solute, and β_i means the power-law coefficient of each solute. The

solute elements are mainly Mn and Mg, A_i is 34.8 and 12.1 MPa respectively, and the β_i is 0.9 and 1.14 respectively. The contents of Mn and Mg in the alloy powder used account for 4.77% and 1.37%, respectively. With the help of the rapid solidification of the SLM process, a large part of Mn and matrix form a solid solution to strengthen the alloy [27]. The strength increased by solid solution strengthening is calculated to be about 143 MPa, which accounts for ~44% of the total yield strength.

There are four types of precipitation strengthening, i.e., order strengthening $\Delta\sigma_{\rm ord}$, coherency strengthening $\Delta\sigma_{\rm coh}$, modulus mismatch strengthening $\Delta\sigma_{\rm mod}$, and Orowan strengthening $\Delta\sigma_{\rm or}$ [9]. As shown in Figs. 13(a, b), there are a few dislocations in the grain and the precipitated phase is relatively coarse, with an average diameter of about 82 nm. Therefore, the main precipitation strengthening mechanism in this study is the Orowan mechanism. The Orowan strengthening mechanism is calculated by [28]:

$$\Delta\sigma_{\rm Or} = M \frac{0.4}{\pi} \frac{Gb}{\sqrt{1-v}} \frac{\ln\left(\frac{\pi d_{\rm m}}{4b}\right)}{\lambda} \tag{3}$$

$$\lambda = \left(\frac{1}{2}\sqrt{\frac{2\pi}{3\phi}} - 1\right)\frac{\pi d_{\rm m}}{4} \tag{4}$$

where M(=3.06) is the average matrix orientation factor of Al, b(=0.286) nm is the size of the matrix Burgers vector, ϕ (=0.99%) is the volume fraction of precipitated phase [29], G(=27.8) GPa is the shear modulus of Al [30], λ is the effective particle spacing, $d_{\rm m}$ is the average precipitate diameter, and v=0.331 is the Poisson's ratio for Al [31]. Through calculation, the precipitation strengthening is about 48 MPa, accounting for 15% of the total yield strength.

According to the Hall-Petch relationship [3]:

$$\sigma_{\mathbf{y}} = \sigma_0 + kD^{-1/2} \tag{5}$$

where σ_0 (=20 MPa) is the intrinsic resistance of the lattice to dislocation motion, k is the constant representing the relative strengthening contribution from grain boundaries, and D is the average grain boundary diameter. For Al alloys, k is usually taken to be 0.14 MN/m^{3/2}. And the yield strength is dependent on the average grain boundary diameter. According to TEM results, it can be found that the

grains are very fine in the SLMed alloys. The average grain size is about 1.56 µm. Therefore, fine grain strengthening or grain boundary strengthening is pronounced in the studied alloys. The strength contribution of each strengthening mechanism is shown in Table 4. The contribution of solution strengthening and grain boundary strengthening to yield strength is about 275 MPa (85%). Therefore, the main strengthening mechanisms of SLM aluminum alloy are solution strengthening and grain boundary strengthening.

 Table 4
 Strength contribution from different strengthening mechanisms

Strengthening mechanism	Strength/ MPa	Proportion/
Solution strengthening	143	44
Precipitation strengthening	48	15
Grain boundary strengthening	132	41

5 Conclusions

- (1) The new Al–Mn–Mg–Sc–Zr alloys prepared in the energy density range of 104–143 J/mm³ have stable properties and similar microstructure. They have fine grains and a few defects and coarse intermetallics. The yield strength is 335–338 MPa, the tensile strength is 397–400 MPa, and the elongation is all above 11%. When the energy density is higher than 152 J/mm³, the elongation decreases sharply.
- (2) EBSD and micro-texture results show that the SLM alloys consist of columnar grains and equiaxed grains. The columnar grains have an obvious preferred orientation, while equiaxed grains orient randomly. The SLM alloy with predominant columnar grains has a stronger texture than the alloy with predominant equiaxed grains.
- (3) The quantitative calculation results show that the main strengthening mechanisms of SLM aluminum alloy are solution strengthening and grain boundary strengthening, which account for 44% and 41% of the total yield strength, respectively. Precipitation strengthening from the AlFeMnScZr phase accounts for 15%.

Acknowledgments

This work was financially supported by the Natural Science Foundation of Hunan Province (Nos. 2020JJ4114, 2016JJ3151), the National Natural Science Foundation of China (No. 51601229), the Young Elite Scientist Sponsorship Program by CAST (No. 2015QNRC001), the Hunan Province Innovation Platform and Talent Plan Project, China (No. 2015RS4001) and the Open-End Fund for the Valuable and Precision Instruments of Central South University, China (No. CSUZC201815).

References

- [1] SZOST B A, TERZI S, MARTINA F, BOISSELIER D, PRYTULIAK A, PIRLING T, HOFMANN M, JARVIS D J. A comparative study of additive manufacturing techniques: Residual stress and microstructural analysis of CLAD and WAAM printed Ti-6Al-4V components [J]. Materials & Design, 2016, 89: 559-567.
- [2] HERDERICK E D. Progress in additive manufacturing [J]. Journal of Metals, 2015, 67(3): 580–581.
- [3] SHI Yun-jia, YANG Kun, KAIRY S K, PALM F, WU Xin-hua, ROMETSCH P A. Effect of platform temperature on the porosity, microstructure and mechanical properties of an Al-Mg-Sc-Zr alloy fabricated by selective laser melting [J]. Materials Science and Engineering A, 2018, 732: 41-52.
- [4] LIU Zhan-qi, MA Rui-xin, XU Guo-jian, WANG Wen-bo, SU Yun-hai. Effects of annealing on microstructure and mechanical properties of γ-TiAl alloy fabricated via laser melting deposition [J]. Transactions of Nonferrous Metals Society of China, 2020, 30(4): 917–927.
- [5] HUANG S H, LIU P, MOKASDAR A, HOU L. Additive manufacturing and its societal impact: A literature review [J]. The International Journal of Advanced Manufacturing Technology, 2013, 67: 1191–1203.
- [6] CAMPBELL I, BOURELL D, GIBSON I. Additive manufacturing: Rapid prototyping comes of age [J]. Rapid Prototyping Journal, 2012, 18(4): 255–258.
- [7] XIAO Quan-feng, HUANG Ji-wu, JIANG Ying-ge, JIANG Fu-qing, WU Yun-feng, XU Guo-fu. Effects of minor Sc and Zr additions on mechanical properties and microstructure evolution of Al–Zn–Mg–Cu alloys [J]. Transactions of Nonferrous Metals Society of China, 2020, 30(6): 1429–1438.
- [8] JU Jiang, LI Jing-jing, JIANG Min, LI Meng-ya, YANG Li-xiang, WANG Kai-ming, YANG Chao, KANG Mao-dong, WANG Jun. Microstructure and electrochemical corrosion behavior of selective laser melted Ti-6Al-4V alloy in simulated artificial saliva [J]. Transactions of Nonferrous Metals Society of China, 2021, 31(1): 167-177.
- [9] JAVAID M, HALEEM A, SINGH R P, SUMAN R, RAB S. Role of additive manufacturing applications towards environmental sustainability [J]. Advanced Industrial and Engineering Polymer Research, 2021, 4(4): 312–322.
- [10] RAO S, CUNNINGHAM R, OZTURK T, ROLLETT A D. Measurement and analysis of porosity in Al-10Si-1Mg components additively manufactured by selective laser melting [J]. Materials Characterization, 2016, 5: 701-716.
- [11] READ N, WANG W, ESSA K, ATTALLAH M M. Selective

- laser melting of AlSi10Mg alloy: Process optimization and mechanical properties development [J]. Materials and Design, 2015, 65: 417–424.
- [12] LIU Zhi-yuan, ZHAO Dan-dan, WANG Pei, YAN Ming, YANG Can, CHEN Zhang-wei, LU Jian, LU Zhao-ping. Additive manufacturing of metals: Microstructure evolution and multistage control [J]. Journal of Materials Science & Technology, 2022, 100: 224–236.
- [13] BAYOUMY D, SCHLIEPHAKE D, DIETRICH S, WU X H, ZHU Y M, HUANG A J. Intensive processing optimization for achieving strong and ductile Al–Mn–Mg–Sc–Zr alloy produced by selective laser melting [J]. Materials & Design, 2021, 198: 109317.
- [14] CHEN Jing, HOU Wei, WANG Xiu-zhuan, CHU Song-lin, YANG Zhi-yi. Microstructure, porosity and mechanical properties of selective laser melted AlSi10Mg [J]. Chinese Journal of Aeronautics, 2020, 33(7): 2043–2054.
- [15] KEMPEN K, THIJS L, van HUMBEECK J, KRUTH J P. Processing AlSi10Mg by selective laser melting: Parameter optimization and material characterization [J]. Materials Science and Technology, 2015, 31(8): 917–923.
- [16] LI Rui-di, WANG Min-bo, YUAN Tie-chui, SONG Bo, CHEN Chao, ZHOU Ke-chao, CAO Peng. Selective laser melting of a novel Sc and Zr modified Al–6.2Mg alloy: Processing, microstructure, and properties [J]. Powder Technology, 2017, 319: 117–128.
- [17] WU Hong, REN Yao-jia, REN Jun-ye, LIANG Lu-xin, LI Rui-di, FANG Qi-hong, CAI An-hui, SHAN Quan, TIAN Ying-tao, BAKER I. Selective laser melted AlSi10Mg alloy under melting mode transition: Microstructure evolution, nanomechanical behaviors and tensile properties [J]. Journal of Alloys and Compounds, 2021, 873: 159823.
- [18] LI Lan-bo, LI Rui-di, YUAN Tie-chui, CHEN hao, ZHANG Zhi-jian, LI Xiao-feng. Microstructures and tensile properties of a selective laser melted Al-Zn-Mg-Cu (Al7075) alloy by Si and Zr microalloying [J]. Materials Science & Engineering A, 2020, 787: 139492.
- [19] CIURANA J, HERNANDEZ L, DELGADO J. Energy density analysis on single tracks formed by selective laser melting with CoCrMo powder material [J]. The International Journal of Advanced Manufacturing Technology, 2013, 68: 1103–1110.
- [20] ZHENG Li-jing, LIU Ying-ying, SUN Shao-bo, ZHANG Hu. Selective laser melting of Al-8.5Fe-1.3V-1.7Si alloy: Investigation on the resultant microstructure and hardness [J]. Chinese Journal of Aeronautics, 2015, 28(2): 564-569.
- [21] OLAKANMI E O, COCHRANE R F, DALGARNO K W. Densification mechanism and microstructural evolution in selective laser sintering of Al–12Si powders [J]. Journal of Materials Processing Technology, 2010, 211(1): 113–121.
- [22] LI X P, WANG X J, SAUNDERS M, SUVOROVA A, ZHANG L C, LIU Y J, FANG M H, HUANG Z H, SERCOMBE T B. A selective laser melting and solution heat treatment refined Al–12Si alloy with a controllable ultrafine eutectic microstructure and 25% tensile ductility [J]. Acta Materialia, 2015, 95: 74–82.
- [23] LI Ping, LI Rui-di, YANG Hai-ou, YUAN Tie-chui, NIU Peng-da, WANG Min-bo, LI Lan-bo, CHEN Chao. Selective

- laser melting of Al-3.48Cu-2.03Si-0.48Sc-0.28Zr alloy: Microstructure evolution, properties and metallurgical defects [J]. Intermetallics, 2021, 129: 107008.
- [24] WANG Zi-hong, LIN Xin, KANG Nan, HU Yun-long, CHEN Jing, HUANG Wei-dong. Strength-ductility synergy of selective laser melted Al-Mg-Sc-Zr alloy with a heterogeneous grain structure [J]. Additive Manufacturing, 2020, 34: 101260.
- [25] HU Hong-wei, DING Xue-ping, WANG Lin-zhi. Numerical analysis of heat transfer during multi-layer selective laser melting of AlSi10Mg [J]. Optik, 2016, 127(20): 8883–8891.
- [26] RYEN Ø, HOLMEDAL B, NIJS O, NES E, SJÖLANDER E, EKSTRÖM H E. Strengthening mechanisms in solid solution aluminum alloys [J]. Metallurgical and Materials Transactions A, 2006, 37(6): 1999–2006.
- [27] JIA Qing-bo, ROMETSCH P, KÜRNSTEINER P, CHAO Qi, HUANG Ai-jun, WEYLAND M, BOURGEOIS L, WU

- Xin-hua. Selective laser melting of a high strength AlMnSc alloy: Alloy design and strengthening mechanisms [J]. Acta Materialia, 2019, 171: 108–118.
- [28] WU L M, WANG W H, HSU Y F, TRONG S. Effects of homogenization treatment on recrystallization behavior and dispersoid distribution in an Al–Zn–Mg–Sc–Zr alloy [J]. Journal of Alloys and Compounds, 2008, 456: 163–169.
- [29] VO N Q, DUNAND D C, SEIDMAN D N. Improving aging and creep resistance in a dilute Al–Sc alloy by microalloying with Si, Zr and Er [J]. Acta Materialia, 2014, 63: 73–85.
- [30] KENDIG K L, MIRACLE D B. Strengthening mechanisms of an Al-Mg-Sc-Zr alloy [J]. Acta Materialia, 2002, 50: 4165-4175.
- [31] KRUG M E, MAO Z, SEIDMAN D N, DUNAND D C. Comparison between dislocation dynamics model predictions and experiments in precipitation-strengthened Al-Li-Sc alloys [J]. Acta Materialia, 2014, 79: 382-395.

不同选择激光熔化工艺参数下 Al-4.77Mn-1.37Mg-0.67Sc-0.25Zr 合金的 拉伸性能及显微组织

赖 毅1, 邓 英1,2, 朱鑫文1, 郭一帆1, 徐国富1,2, 黄继武1, 尹志民1

- 1. 中南大学 材料科学与工程学院,长沙 410083;
- 2. 中南大学 粉末冶金国家重点实验室,长沙 410083

摘 要:采用选择激光熔化(SLM)技术在不同工艺参数下制备 Al-4.77Mn-1.37Mg-0.67Sc-0.25Zr 合金(质量分数,%),通过拉伸试验和显微观察研究合金的组织和力学性能。结果表明:当能量密度为 104~143 J/mm³ 时,力学性能保持相对稳定;屈服强度为 335~338 MPa,抗拉强度为 397~400 MPa,伸长率均在 11%以上。在此能量密度区间内,SLM 合金缺陷和粗大金属间化合物较少,与此同时,有大量细小的 AlFeMnScZr 相析出。当能量密度超过 152 J/mm³ 时,可以观察到一些孔洞和裂纹,且伸长率急剧下降。定量计算结果表明,该合金固溶强化、晶界强化和析出强化占比分别为 44%、41%和 15%。

关键词: 选择激光熔化; 铝合金; 拉伸性能; 强化机制; 显微组织

(Edited by Xiang-qun LI)